Transport properties of HfO_{2-x} based resistive-switching memories

Zhongrui Wang,[1] HongYu Yu,[2,*] Xuan Anh Tran,[1] Zheng Fang,[1] Jinghao Wang,[3] and Haibin Su[3,*]
[1]*School of Electrical and Electronic Engineering, Nanyang Technological University, Singapore 639798*
[2]*South University of Science and Technology of China, China 518055*
[3]*School of Materials Science, Nanyang Technological University, Singapore 639798*
(Received 1 October 2011; revised manuscript received 16 February 2012; published 22 May 2012)

Transport measurements of both the dc and the low-frequency ac are performed on Pt/HfO_{2-x}/TiN resistive-switching memory cells at various temperatures. The conductance of the pristine cells has a power law $\omega^S T^N$ relationship with temperature and frequency. To account for the much larger conductance of both the high resistance states (HRSs) and the low resistance states (LRSs), an additional conductance term associated with oxygen vacancy filaments is added, which is independent of the cross-sectional area of the memory cell. This additional component of conductance in a HRS is frequency independent but temperature dependent, showing the small polaron originated transport, with an activation energy of 50 (2.1) meV at temperatures above (below) half of the Debye temperature, which agrees with the analysis of the electric field dependence data. The frequency- and temperature-dependent conduction of HRSs indicate the existence of polarization centers which facilitate the transport and make HfO_{2-x} highly polarizable. However, the additional conductance term associated with filaments in LRS, of an order of $\sim 10^5$ S m^{-1}, exhibits a weak metallic behavior in temperature-dependent measurements. Properties of aligned oxygen vacancy chains on the $(\bar{1}11)$ surface are calculated by first-principles simulation. Through analysis of the partial density of states and spatial distribution of the wave function of impurity states generated by oxygen vacancies, this weak metallic behavior is attributed to the delocalization of the impurity band associated with aligned oxygen vacancies.

DOI: 10.1103/PhysRevB.85.195322 PACS number(s): 72.20.−i, 73.20.Hb

I. INTRODUCTION

Resistance switching, which refers to the alternating of the conductance in solids triggered by the external electrical field, is a very fundamental physical phenomena observed since the 1960s.[1] Subsequent studies and reviews started in 1970 have demonstrated its potential application on nonvolatile memory.[2,3] Recently, with the advancement of complementary metal-oxide semiconductor (CMOS) fabrication technology, resistive-switching random access memory (RRAM) has been intensively studied[4,5] and is considered one of the candidates of next-generation nonvolatile memory due to high programming speed, CMOS compatibility, and ease of fabrication.[6] Materials showing stable resistive switching include metal oxides (especially transition-metal oxides such as HfO_2, NiO, and TiO_2), metal sulfides, metal nitrides, and carbon based materials.

Among these materials, HfO_2 based RRAM has been widely reported. As HfO_2 is widely used in transistor gate dielectric stack, its resistive-switching characteristics are of great importance to both memory and logic circuit applications. Various HfO_2 based capacitor structures have been reported with resistive-switching behaviors.[7] Popular explanations on current transport include Schottky barrier modification at electrodes, migration of electrode ions (impurity metal ions diffusion), space-charge-limited current, Mott's variable range hopping via defect states, and filamentation by ordered oxygen deficiency.[8–13] However, there is no unified mechanism of transport and switching developed for RRAM. For different systems, there are different kinds of interpretations.

For valence change mechanism and thermal chemical mechanism based redox RRAM, recent physical characterization studies on HfO_{2-x},[14] NiO_{1-x},[15,16] SiO_{2-x},[17] $SrTiO_{3-x}$,[18] and TiO_{2-x}[12,13,19] have provided evidence of the existence of dielectric breakdown induced oxygen vacancies. Electronic properties of these materials are very sensitive to local configurations of oxygen vacancies.[20,21] Reviews of oxygen vacancy percolations in redox RRAM have been made by Waser,[22] Akinaga,[23] Kügeler,[24] and Szot.[25] According to the oxygen vacancy percolation scenario, the low resistance state (LRS) is formed by an oxygen deficient percolation path stochastically which connects the anode and cathode. However, the filament is ruptured or partially ruptured in the high resistance state (HRS) because oxygen ions drift back and recombine with oxygen vacancies. Considering that point defects tend to segregate at grain boundaries and surfaces where diffusion barriers are lower,[26–29] effective pathways of oxygen vacancy should be along grain boundaries or surfaces.

But the role of oxygen vacancies in electron transport is not clear in HfO_{2-x} based RRAM. HfO_{2-x} is a highly polarizable medium where carriers in intrinsic HfO_{2-x} will be self-trapped by forming polarons.[30,31] In this work, we take low-frequency ac conductivity measurements at various temperatures to probe the electronic properties of filaments. Both HRS and LRS cells are of an additional frequency-independent conductance term despite the power-law term inherited from pristine cells. For HRS cells, such a term is strongly temperature dependent, while for LRS cells the temperature dependence is much weaker. The HRS conduction can be well described by small polaron hopping in a temperature range above half of the Debye temperature, and LRS exhibits a weak metallic nature. First-principles simulation has been performed to analyze oxygen vacancies on the surface of HfO_{2-x}. $(\bar{1}11)$ and (111) surfaces are relatively stable among various facets. The formation energy of oxygen vacancy in the vicinity of the surface is lower than that in the bulk. One stable oxygen vacancy configuration is shown to align in the [101]

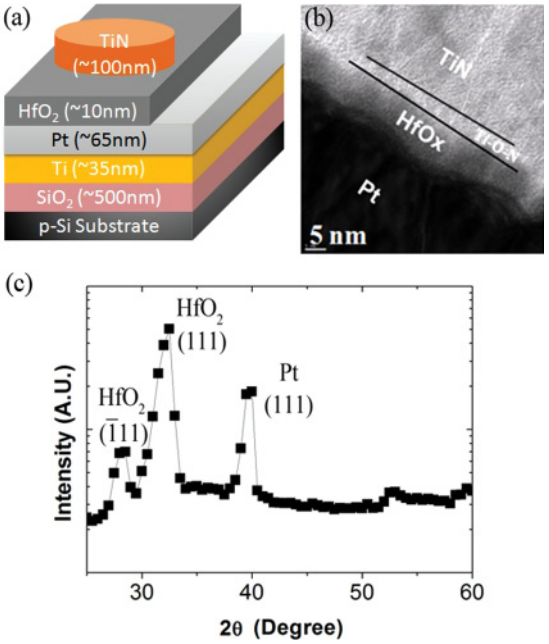

FIG. 1. (Color online) (a) Schematic illustration of a Pt/HfO_{2-x}/TiN RRAM cell structure. (b) Cross-sectional HRTEM image. The TiO_xN_y interfacial layer can be identified. (c) XRD of a HfO_{2-x} RRAM cell. HfO_{2-x} is of the polycrystalline phase. Dominant phases are ($\bar{1}11$) and (111).

direction. The weak metallic nature of LRS results from the delocalization of the impurity state with t_{2g} character inside the band gap.

II. SAMPLE PREPARATION AND PHYSICAL CHARACTERIZATION

The HfO_{2-x} RRAM cells in this study are of the structure shown in Fig. 1(a). The Pt bottom electrode is deposited by radio frequency sputtering onto the Ti adhesion layer. The sputtered Hf is annealed in oxygen ambient for 5 min. at 450 °C to form the switching HfO_{2-x} layer with a thickness of ~10 nm as revealed by high-resolution transmission electron microscopy (HRTEM) [see Fig. 1(b)]. Top electrodes are produced by patterning the reactive sputtered 100 nm TiN film with a diameter ranging from 100 μm to 500 μm. A Keithley 4200-CVU semiconductor analyzer carries both low-frequency (1 KHz to 1 MHz) and dc characterization with the aid of a SUSS cryogenic probing system cooled by liquid helium.

The HRTEM image [see Fig. 1(b)] shows the formation of a TiO_xN_y interfacial layer between the HfO_{2-x} and TiN in an as-deposited device, which has also been reported by Jorel.[32] This interfacial layer may serve as an oxygen reservoir which can absorb and release oxygen ions during the switching process.

X-ray diffraction (XRD) taken on HfO_{2-x} without TiN top gate cells indicates a polycrystalline nature of the dielectric film. ($\bar{1}11$) and (111) are the dominant phases with strong peaks [see Fig. 1(c)].[33]

Repeatable switching behaviors have been demonstrated in our previous study.[34] The pristine cells have a typical forming voltage around 5 V. The LRS cells can be reset to an HRS by applying a negative voltage on the top TiN electrode. Typical reset voltage is ~ -2.5 V. To set the cells again to LRS, an average set voltage of ~1.5 V is desired. The on/off ratio is around 100. More than 10^3 cycles of switching have been achieved by using dc sweep. The retention of data at 120 °C lasts for $>10^4$ s.

III. RESULTS AND DISCUSSION

A. Room-temperature dielectric response

The admittance Y is typically written as the sum of conductance G and susceptance B multiplied by the imaginary unit i.

$$Y = G(\omega,T) + iB(\omega,T) = G(\omega,T) + i\omega C(\omega,T). \quad (1)$$

Here $G(\omega,T)$ is the function of angular velocity ω at temperature T, while $B(\omega,T)$ can be alternatively expressed as the product of equivalent capacitance $C(\omega,T)$ and angular velocity ω.

1. Pristine state

For pristine cells, as shown in Fig. 2(a), it shows a typical non-Debye response commonly observed in polycrystalline/amorphous semiconductors, which is also regarded as the Curie–von Schweidler's behavior described by Eq. (2).[35,36]

$$G(\omega,T) = G_{\text{const}}\omega^{S(\omega,T)}T^{N(\omega,T)}, \quad (2)$$

where G_{const} is a real constant. Under constant temperature conditions, the conductance equation can be simplified [see Eq. (3)]:

$$G(\omega) = G_0\omega^{S(\omega)}. \quad (3)$$

This behavior has been reported for HfO_{2-x} and TiO_{2-x} dielectric thin-film devices in recent years.[37–39] The origin of this non-Debye-type response comes from localized states deep within the principal band gap. The formation of these states results from the disorder, such as dislocations, impurities, or oxygen vacancies. Under paired sites approximation, electrons confined in these localized states can shuttle between the nearest-neighboring localized states and the original states under an external periodic electric field. The exponents S and N in Eq. (2) are functions of both frequency and temperature, and their frequency and temperature dependence are strongly related to the underlying charge transport mechanism, which characterizes the nonlinear dependence of $\ln(G)$ on $\ln(\omega)$ and $\ln(T)$ at the specified temperature and frequency. Historically, the admittance with exponent S was first reported by Pollak[40] and adopted by subsequent studies.[35,36,41–44] The temperature exponent N was introduced by Long.[35] Systematic reviews of the power law described in Eq. (2) were given by Long and Elliot where theoretical formulations were provided.[35,36] According to Long, a very possible scenario of the dielectric loss in an amorphous or polycrystalline semiconductor is electrons traveling between two neighboring defect sites under an applied periodic electric field. With the partition function constructed for this grand canonical ensemble, the rate equation in equilibrium is established.[35] The effect of the external field is modeled by introducing a small perturbation which

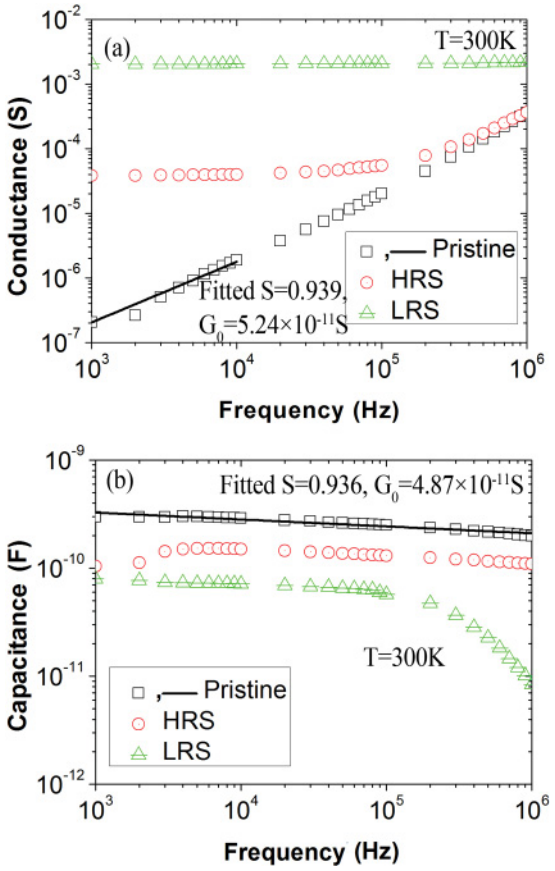

FIG. 2. (Color online) (a) Typical room-temperature ($T = 300$ K) conductance G of pristine, high resistance state, and low resistance state cells in frequency f range 1 KHz–1 MHz. The solid blank line is based on numerical fitting of Eq. (3). (b) Typical room-temperature ($T = 300$ K) equivalent capacitance C ($C = \mathrm{Im}(Y)/\omega$) of pristine, high resistance state and low resistance state cells in frequency f range 1 KHz–1 MHz. The solid blank line is based on numerical fitting of Eq. (4). The fitted S and G_0 are in agreement with those in (a).

changes the equilibrium occupation probability of two sites. Fourier-transformed conductivity is expressed as a function of ω, E_1, E_2, and $\tau(R, E_1, E_2)$, where ω is the frequency, E_1 and E_2 are the energies of electrons localized in the neighboring sites, and τ is the relaxation time which depends on the nature of transport (i.e., correlated barrier hopping, tunneling, small polaron tunneling, or large polaron tunneling).[35] Suggesting empirical forms of $\tau(R, E_1, E_2)$, the frequency and temperature dependence of $S(\omega, T)$ and $N(\omega, T)$ have been calculated for different types of charge transport by Long and Elliot.[35,36] A more specific formulation of dielectric loss caused by small polaron adiabatic hopping was given by Emin, which will be presented in the following section.[45] At room temperature, in a low-frequency regime ($f < 1$ MHz), the frequency exponent S is appropriate to be approximated as a constant with a value between 0 and 1. In this case, the imaginary part of the admittance [or equivalently, $C = \mathrm{Im}(Y)/\omega$] can be calculated by Kramers-Kronig transform.[35,36,40,41]

$$C = G_0 \omega^{S-1} \tan\left(\frac{S\pi}{2}\right). \tag{4}$$

The fitted S of the pristine state cell is 0.936. This agrees with the fitting of conductance G based on Eq. (3) where the fitted S equals 0.939 [see Figs. 2(a) and 2(b)]. The fitted prepower factor G_0 is consistent also.

The area dependence of dielectric response has been investigated. The mean value of exponent S of five random cells is ~0.906, fitted in the frequency range from 1 KHz to 10 KHz, consistent with literature (see Table I).[9,10,37–39] The capacitance is thus slightly decreasing with frequency. The reason for fitting in a very low-frequency range [see Fig. 2(a)] is to avoid increasing external circuit influence with frequency. The presence of very large S (~2) and fast decreasing capacitance when the frequency approaches 1 MHz has been reported.[10,38] Such a parasitic effect lies on contacts as derived by Gonon.[38] The parasitic effects on HRS and LRS capacitance and numerical fitted equivalent circuits are discussed in the next section on equivalent circuits. Another feature of the pristine cell is that its conductance G has area dependence. As shown in Table I, G_0 increases with area. Ideally it scales linearly with area. The observed deviations may be due to the nonuniform sputtered HfO_{2-x} thin film.

The pristine cell has a non-Ohmic dc I-V characteristic. For a $D = 100$ μm cell, its resistance is typically $10^7\Omega$–$10^9\Omega$ at 1 V, which corresponds to a bulk resistivity ~10^8 Ω m representing an insulating dielectric nature.

2. *High resistance state and low resistance state*

The conductance of HRS cells differs from that of pristine cells by including a frequency-independent component $G_{\mathrm{dc,HRS}}(T)$.[39]

$$G(\omega, T) = G_{\mathrm{dc,HRS}}(T) + G_0 \omega^{S(\omega,T)} T^{N(\omega,T)}. \tag{5}$$

Its frequency independence makes a direct contribution to dc conduction, which results in a larger leakage current than that of pristine cells.

TABLE I. Fitted room-temperature ($T = 300$ K) conductance G parameters for pristine, high resistance state and low resistance state cells with diameters ranging from 100 to 500μm. G_0 shows significant area dependence while $G_{\mathrm{dc,HRS}}$ and $G_{\mathrm{dc,LRS}}$ do not have evident area dependence [see Eqs. (3), (5), and (7)].

Diameter (μm)	S	G_0 (S)	$G_{\mathrm{dc,HRS}}$ (S)	$G_{\mathrm{dc,LRS}}$ (S)
100	0.959	2.30×10^{-11}	1.01×10^{-5}	2.26×10^{-3}
200	0.859	2.93×10^{-10}	1.26×10^{-5}	1.44×10^{-3}
300	0.939	3.51×10^{-10}	1.50×10^{-5}	1.39×10^{-3}
400	0.872	1.21×10^{-9}	9.94×10^{-6}	1.19×10^{-3}
500	0.903	1.45×10^{-9}	1.50×10^{-5}	2.27×10^{-3}

The capacitance of the HRS cell is slightly below that of the pristine cell, consistent with literature.[10,38,39] The difference between HRS capacitance and that of the pristine cell most probably comes from contacts influence. In a measurement setup, it is inevitable to have an external resistance R_{external} in series with the dielectric thin film. This causes the reduction in $\text{Im}(Y)$ according to Eq. (6). (The other external circuit component, L_{external}, is neglected here.) It can be seen that the smaller the HRS film resistance R_{HRS}, the larger the reduction in capacitance. A more detailed circuit model with numerical fitting is presented in the next section.

$$C_{\text{HRS}} = \frac{\text{Im}(Y)}{\omega} = \frac{\omega C}{\left(\frac{R_{\text{external}}}{R_{\text{HRS}}} + 1\right)^2 + (\omega C R_{\text{external}})^2}. \quad (6)$$

In contrast with G_0, the $G_{\text{dc,HRS}}(T)$ has no significant area dependence (see Table I) A possible scenario is that the frequency-independent component $G_{\text{dc,HRS}}(T)$ is caused by the partially ruptured filament which has no area dependence. It is also noticed that the value of $G_{\text{dc,HRS}}(T)$ is relatively random. This may originate from the fact that the formation and rupture of the filament is not controllable.

Similar to HRSs, the conductance of LRSs can be described as the sum of a frequency-independent term and a non-Debye response term.

$$G(\omega,T) = G_{\text{dc,LRS}}(T) + G_0\omega^{S(\omega,T)}T^{N(\omega,T)}. \quad (7)$$

In the frequency range from 1 KHz to 1 MHz, the dc component may be much larger than the second term [see Fig. 2(a)]. This simply results in an overall frequency-independent response:

$$G(\omega,T) \cong G_{\text{dc,LRS}}(T). \quad (8)$$

The capacitance of the LRS cell is of similar magnitude with the HRS cell and pristine cell.[10,38,39] The same as the HRS case, the lowering of the overall capacitance compared with the pristine cell is caused by contacts (i.e., external resistance in series with dielectric film). Since $G_{\text{dc,LRS}}(T)$ is much larger than $G_{\text{dc,HRS}}(T)$, the lowering of the capacitance is more apparent than that of HRS. This leads to an even smaller $\text{Im}(Y)$ in LRS. The rapid decrement near 1 MHz proves the existence of the external inductance L_{external} in series with the dielectric film, which is investigated by numerical fitting in the next section also.[8,24]

$G_{\text{dc,LRS}}(T)$ has no clear area dependence, the same as for HRS cells. In literature, filamentary switching is frequently reported of the area-independent resistance in the LRS of the VCM redox RRAM. However, the transport process in the HRS is not simply determined by the filament. Both area-dependent and area-independent HRS resistance have been reported for the HfO_{2-x} based RRAM. (See, for instance, the strong area-dependent HRS resistance that has been witnessed in TiN/Ti/HfO_2/TiN RRAM,[7] and the weakly area-dependent HRS resistance that has been seen in Pt/ZrO_2/HfO_x/TiN RRAM.[46]) This probably relies on the competition between current contribution from the ruptured (or shrunken) filament and the rest of the interface. In our work, both the HRS and LRS of Pt/HfO_{2-x}/TiN show area-independent resistance which is dominated by filament based transport.

3. Equivalent circuit model

In the room-temperature Cole-Cole plot, the pristine cell has a typical nonideal capacitor behavior since amorphous and polycrystalline dielectrics follow the universal power law given by Eq. (3) (see Fig. 3). As mentioned in the previous section, this constant exponent S assumption is appropriate in the low-frequency range. With consideration of the Kramers-Kronig relation, the impedance of ideal pristine cell Z_{CPD} is given by

$$Z_{\text{CPD}} = \frac{1}{G_{\text{pristine}}} = \frac{1}{G_0\omega^S + i\omega C} = \frac{1}{G_0\omega^S + iG_0\omega^S \tan\left(\frac{S\pi}{2}\right)} = \frac{\cos\left(\frac{S\pi}{2}\right)}{G_0\omega^S} e^{i[-(S\pi/2)]}. \quad (9)$$

Since its phase $(-\frac{S\pi}{2})$ is only exponent S dependent and S is constant in the frequency range of experiment, the phase is therefore a constant. Such a device is also referred as a constant phase device (CPD). However, in equivalent circuit modeling, an ideal CPD could not well describe the low-frequency response of the HfO_{2-x} thin film. This is

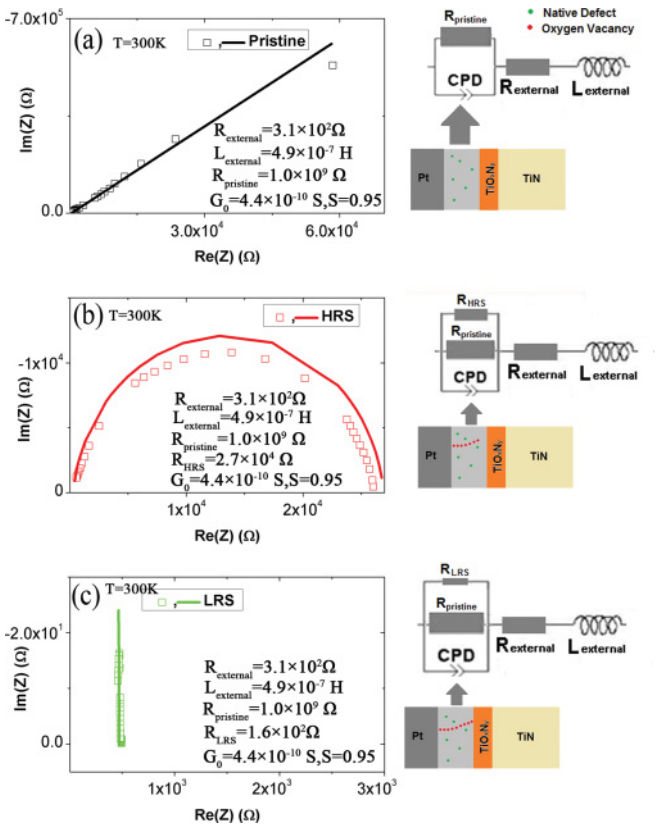

FIG. 3. (Color online) (a) Room-temperature ($T = 300$ K) Cole-Cole plot of a pristine cell in frequency f range 1 KHz–1 MHz. The solid line is based on fitting with the equivalent circuit. The schematic shows the possible scenario in HfO_{2-x}. (b) Room-temperature ($T = 300$ K) Cole-Cole plot of a high resistance state cell in frequency f range from 1 KHz to 1 MHz. The solid red line is based on fitting with the equivalent circuit. (c) Room-temperature ($T = 300$ K) Cole-Cole plot of a low resistance state cell with frequency f range from 1 KHz to 1 MHz. The solid green line is based on fitting with the equivalent circuit.

because an ideal CPD has no dc conductance, which is revealed by Eq. (10):

$$\mathrm{Re}[G(\omega)]|_{\omega=0} = G_0\omega^S|_{\omega=0} = 0. \quad (10)$$

In reality, dc leakage current is inevitable in the HfO_{2-x} thin film. Thus, a parallel resistor is included to model the dielectric film. For the pristine HfO_{2-x} cell, the main source of dc leakage current comes from native defects. For the HfO_{2-x} cell in LRS, the percolation of oxygen vacancies is responsible for dc leakage current, and most probably dc leakage in HRS is caused by a partially ruptured filament. These scenarios are summarized in Fig. 3. As shown in Fig. 3(a), a resistor, R_{pristine}, is in parallel with CPD to account for all dc leakage currents in the nonideal dielectric film. Contact influence is absorbed by a resistor, R_{external}, and an inductor, L_{external}, which are in series with the dielectric film. For the pristine cell, this contact influence is limited because of the very large R_{pristine}. The Cole-Cole plot of the pristine cell shows a straight line in the corresponding frequency range. However, HRS and LRS cells are of small parallel resistance R_{HRS} and R_{LRS}, which are the reciprocals of $G_{\mathrm{dc,HRS}}$ and $G_{\mathrm{dc,LRS}}$, respectively [see the inset of Figs. 3(b) and 3(c), $G_{\mathrm{dc,HRS}} = 1/R_{\mathrm{HRS}}$ and $G_{\mathrm{dc,LRS}} = 1/R_{\mathrm{LRS}}$]. Thus, their electrical performance is more likely to be affected by R_{external} ($\sim$310 Ω) and L_{external} ($\sim 5 \times 10^{-7}$ H), consistent with reported R_{external} for cells with a similar cross-sectional area which ranges from $\sim$4.5 Ω to $\sim$1000 Ω.[47–49] For instance, ideal HRS cells should have a semicircle curve in the complex impedance plane. However, due to external inductance L_{external}, the circle center falls slightly below the x axis.[47–49]

The fitted S for a CPD is 0.94 (see Fig. 3). This is consistent with the previous fitting where $S = 0.936$ [based on Eq. (4)] or 0.939 [based on Eq. (3)]. The fitted G_0 is also of a similar value with the previous fitting which does not include the effect from contact resistance and inductance (see Fig. 2).

The fitted HRS and LRS resistances are 2.7×10^4 Ω and $1.6 \times 10^2 \Omega$, respectively [see Figs. 3(b) and 3(c)]. If the diameter of the cross section of a filament is considered to be several tens of nanometers, the resistivity of the LRS filaments will be $\sim 10^{-5} \Omega$ m, which is in the range of amorphous metal resistivity. On the other hand, the resistivity of HRS filaments is about $10^{-3} \Omega$ m, which implies HRS filaments are more semiconductor-like.[18]

B. Temperature-dependent dielectric response

Although temperature-dependent I-V characteristics have been reported with a HRS/LRS in HfO_{2-x},[34,38] there is no systematical study on the temperature-dependent dielectric response of a HRS/LRS in HfO_{2-x}, by which, the experimental significance of small polaron hopping in HRSs and delocalization of the impurity band of oxygen vacancies in LRSs are observed.

1. Pristine state

For a pristine sample, as a typical polycrystalline/amorphous material, its temperature dependence has been reviewed by Long[21,22] and Elliot.[35,36] In a low-frequency range, since it is inevitable to have dc leakage current in thin dielectric films, there always exists an R_{pristine} [as illustrated in Fig. 3(a)] which dominates in the low frequency. Depending on the nature of the leakage current, R_{pristine} can have different types of temperature dependence.[21,22] On the contrary, R_{HRS} (or $G_{\mathrm{dc,HRS}}$) and R_{LRS} (or $G_{\mathrm{dc,LRS}}$) are filaments oriented, and their presence is caused by percolation of oxygen vacancies. In the high-frequency range, $G_0\omega^{S(\omega,T)}T^{N(\omega,T)}$ consists of a much larger weight over R_{pristine}. Therefore, a pristine cell shows no difference to a HRS cell. In the high-frequency range (from 100 KHz to 1 MHz, to bypass a potential dc component), it is observed that room-temperature $G_0\omega^{S(\omega,T)}T^{N(\omega,T)}$ has very weak temperature dependence that $G(\omega,T)$ slightly increases with temperature, which is consistent with the observation of HRSs discussed in the next section.

2. High resistance state

Temperature-dependent Cole-Cole plot. The dc I-V curve of HRS cells has significant temperature dependence, as mentioned. However, the origin of this dependence is not clearly specified in previous studies. It has been reported that resistive switching can be due to either bulk filament formation or interface modification.[23] In the interface resistive-switching model, a Schottky barrier is formed between the dielectric layer and metal electrode. The barrier height is affected by the chemical property of the dielectric layer, which results in an overall resistance change.[23] A temperature-dependent Cole-Cole plot is employed to analyze the origin of this temperature dependence that determines whether it is caused by the bulk dielectric film or by the Schottky barrier at the interface [see Fig. 4(a)]. The left interceptions with the x axis of the three curves are all $\sim$165 Ω, indicating a temperature insensitive R_{external} in the equivalent circuit model, which is also observed by Papagianni.[47] Based on the equivalent circuit, this excludes the possibility of Schottky barrier modification in the HfO_{2-x} system, which should be in series with the dielectric film in the equivalent circuit. The contact between HfO_{2-x} and the electrode in a HRS may be of Ohmic type, for the following two reasons. The first reason is that the extracted activation energy of transport is much smaller than the expected Schottky barrier from the band diagram, which will be discussed in the following section [see Fig. 4(b) and the corresponding text]. A similar activation energy has been reported for a Si/HfO_2/TiN system,[50] TiN/HfO_2/Au system,[51] and Al/HfO_2/Si system.[52] The other reason is that the I-V curve is symmetric in Pt/HfO_{2-x}/TiN without a rectifying effect, which could be seen from our previous electrical characterization.[34] Thus, the filament-oriented $G_{\mathrm{dc,HRS}}(T)$ is mainly responsible for the HRS temperature dependence in the Cole-Cole plot.

dc conductance Arrhenius plot. Since $G_{\mathrm{dc,HRS}}(T)$ has a strong temperature dependence, it shows that the transport is facilitated by thermal-activated processes. An Arrhenius plot of dc conductance measured at 10 mV (the same amplitude of the voltage used in ac measurements) is shown in Fig. 4(b). This type of Arrhenius plot is widely observed in polarizable systems where polarons take place. For instance, similar plots have been frequently reported for HfO_{2-x}.[50–52] The curve has two regions with very different slopes. The extracted activation energy of each region is 50 and 2.5 meV as indicated in Fig. 4(b). Compagnoni has reported that the activation

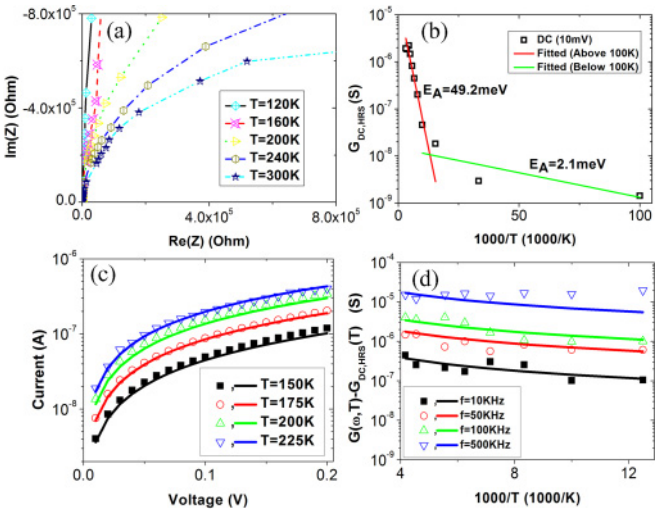

FIG. 4. (Color online) (a) Cole-Cole plot for a high resistance state cell at different temperatures (from 120 to 300 K) which reveals that the switching is not caused by interface Schottky barrier modification. (b) Arrhenius plot of high resistance state dc conductance $G_{\mathrm{dc,HRS}}$ as a function of reciprocal temperature $1000/T$ suggests a small polaron hopping conduction type. (c) I-V of high resistance state cell at different temperature (from 150 K to 225 K). Solid lines are numerical fitting based on a polaron hopping model [$T >$ half Debye temperature; see Eq. (11)]. (d) Arrhenius plot of high resistance state frequency-dependent conductance $G - G_{\mathrm{dc,HRS}}$ as a function of reciprocal temperature $1000/T$ at different frequencies f. Solid lines are fittings, based on Eq. (12), of highly polarizable mediums.

energies are 87 and 60 meV (under reversed biasing) in the high-temperature regime and 5 meV in the low-temperature regime. In other polarizable systems, for instance TiO_2, a similar slope transition is observed at half of its Debye temperature.[53]

The activation energy in the high-temperature regime of a HfO_{2-x} system is of a magnitude of tens of meV,[50,52] which is much smaller than the band gap. Consider the band diagram of a HfO_{2-x} system with oxygen vacancies; since the Fermi level is determined by external electron reservoirs which are Pt and TiN electrodes, the Fermi level will be far below the conduction band.[54] Hence, it is very difficult to directly excite electrons from oxygen-vacancy-induced defect states to the conduction band. One possible way is by electron-type polaron hopping via metal ions in the vicinity of oxygen vacancies. This type of small polaron hopping has been proved to exhibit the same transition of slope depicted in Fig. 4(b) by Schnakenber,[55] and the transition temperature is about half of the Debye temperature because polarons will be frozen out at lower temperatures. For instance, in other group IV transition-metal oxide systems like the TiO_{2-x} system, Yildiz has reported transitions at half of the Debye temperature due to adiabatic hopping of small polarons.[53] The transition temperature is around 100 K in our observation, which is in agreement with half of the HfO_2 Debye temperature of 220($\pm$10) K.[56] It is also noted that, the first-principle simulation calculated adiabatic small polaron hopping energy of 50 meV in the intrinsic HfO_2 system is very close to experimental observations.[30]

Electric field impact on temperature-dependent I-V characteristics. Another experimental observation also reveals the polaron nature of transport in a HRS in a high-temperature region is its electric field influence on temperature-dependent I-V characteristics [see Fig. 4(c)]. In HfO_{2-x}/TiN systems, Poole-Frenkel emission like I-V characteristics is frequently reported in a high-temperature range,[51] which is most probably caused by polaron-related transport in the adiabatic regime rather than direct excitation of electrons to a conduction band as suggested by Emin.[57] Assuming a T^{-1} preexponential factor for adiabatic hopping, dc conductance as a function of field strength F is described by

$$G_{\mathrm{HRS,dc}} \propto \frac{\upsilon}{T} \exp\left[\frac{-E(\infty) + \sqrt{V_L F a \cos\theta}}{k_B}\left(\frac{1}{T} - \frac{1}{T_0}\right)\right], \tag{11}$$

where υ represents the suitable average of atomic vibrational frequencies, a is the diffusion length, $E(\infty)$ is the activation energy for infinitely far separated polarons, F is the magnitude of the electric field driving the hop, and θ is the angle between the applied field and the jump direction. The preexponential T^{-1} has a very limited effect in the high-temperature range, especially for $T > 150$ K.[51] Thus, the conductance of Eq. (11) behaves similarly to that of the ordinary Poole-Frenkel emission in the high-temperature regime, and it well fits with the experimental observations with fitted $E(\infty) = 42$ meV, which is consistent with E_A in Fig. 4(b).

G vs (1000/T) at different frequencies in a high resistance state. As shown in Fig. 4(d), HRS cells exhibit a similar frequency-dependent conductance at low temperature to pristine cells, which is commonly observed in polycrystalline/amorphous semiconductors. The filament contribution $G_{\mathrm{dc,HRS}}(T)$ is frequency independent, and the main contribution to a high-frequency response comes from disorder-induced defects given by $G(\omega,T) - G_{\mathrm{dc,HRS}}(T)$. At a constant temperature, the $G(\omega,T) - G_{\mathrm{dc,HRS}}(T)$ increases with frequency as discussed in Sec. III A2. According to Long, this frequency-dependent conductance is associated with the dielectric response nature of the material.[35] At a fixed angular velocity ω, $[G(\omega,T) - G_{\mathrm{dc,HRS}}(T)]/G_{\mathrm{dc,HRS}}(T)$ decreases with temperature. In other words, the ac contribution to total conductance is larger at low temperature. The physical origin of this phenomenon has been investigated by Emin.[45] At low temperature, the ac polarization requires spontaneous emission of phonons but the dc conduction is governed by thermal assisted hops with high energy barriers. Considering ac conduction at low-frequency and low-temperature regime is associated with a very small fraction of carriers ($\sim$0.1%) in transition-metal oxides, the polarization-paired center is anticipated to play an important role in the transport process. Within each center, carriers can move cooperatively. Nevertheless, the conductance is linear in the reciprocal temperature domain (T ranges from 80 to 250 K). Quantitative formulation of ac polaronic conductance is given by Emin.[45] The approach of Emin differs from that of Long by the formulation of relaxation time. In the approach of Emin, the relaxation time is inversely proportional to the transition rate from one state to the other. By using a deformation model to account for the electrons

interaction with the long-wavelength acoustic phonons, the transition rate is calculated by Fermi's golden rule. This leads to the following expression of dielectric loss:

$$G(\omega,T) - G_{\mathrm{dc,HRS}}(T) = G_0 \frac{\left(\frac{\omega}{\omega_0}\right)\left(\frac{T}{T_0}\right)}{\left[1-\left(\frac{\omega_0}{\omega}\right)^{1/n}\left(\frac{T}{T_0}\right)\right]^2}, \quad (12)$$

where $G_0 \equiv (A/l)2q^2\langle R^2\rangle \rho_2(\mu,0)\omega_0 k_B T_0 \exp[-(n^2/2)]$ and $(\omega_0)^{1/n}/T_0 \equiv 2n^2 k_B \omega^{1/n}/\delta_0$. A is the cross-sectional area, l is the dimension in the direction of current flow, q is the electron charge, R is the separation between polarization-paired sites, $\rho_2(\mu,0)$ is the density of paired sites with local energy μ and no site-to-site energy difference, k_B is Boltzmann's constant, and δ_0 is the peak of a dynamic factor generally rising with ω. At low temperature, $n \to 3$ and $\delta_0 \propto \omega^{1/\beta}$, thus $(\omega_0)^{1/n}/T_0$ is constant. Also, $G_0/\omega_0 T_0$ is constant, too. As shown in Fig. 4(d), the four curves are fitted with $(\omega_0)^{1/n}/T_0|_{n\to 3} = 0.011 s^{-(1/\beta)} K^{-1}$, which follows the predictions made by Emin. It can be further shown that the exponent S derived from Emin's expression is close to unity in the low-frequency range:

$$S(\omega,T) = \frac{\partial\{\ln[G(\omega,T) - G_{\mathrm{dc,HRS}}(T)]\}}{\partial[\ln(\omega)]}\bigg|_{n\to 3} = 1 - \frac{2\left[\frac{(\omega_0)^{1/\beta}}{T_0}\right]T}{3\omega^{1/\beta} - 3\left[\frac{(\omega_0)^{1/\beta}}{T_0}\right]T}. \quad (13)$$

Substituting in the value of $(\omega_0)^{1/n}/T_0|_{n\to 3}$, the S ranges from 0.86 to 0.98 with a mean of 0.95 in the frequency range of the measurement, which is consistent with the room-temperature dielectric loss fitting data shown in Figs. 2 and 3. The corresponding temperature exponent N ranges from 1.0 to 1.4 in the frequency and temperature range of the measurement. The agreement between theorems and experiments indicates the existence of polarization-paired centers in the HfO_{2-x} medium, which makes the dielectric film highly polarizable.[35,36]

3. *Low resistance state sample temperature dependence*

In contrast to HRS cells, LRS cells show a very weak temperature-dependent resistivity. As shown in Fig. 5, the dc resistance is about 122 Ω at 10 K and 139 Ω at 225 K. This phenomenon has also been witnessed in WO_x based RRAM, where the reported resistance is 9 Ω at 10 K and 11 Ω at 300 K.[58] By taking film thickness as 10 nm and a filament diameter of 10 nm, the resistivity is $\sim 10^{-6}$ Ω m. As illustrated by the inset of Fig. 5, I-V curves clearly show Ohmic characteristics. The very low resistance-residue ratio (R_{225K}/R_{10K}) of 1.14, the resistivity of $\sim 10^{-6}$ Ω m, and the Ohmic characteristics all unravel the weak metallic nature of LRSs, which is expected to correlate with percolation of impurity states associated with oxygen vacancies. In literature, Ohmic LRSs are widely reported.[38,51,59] The contact between the HfO_{2-x} and electrode is of an Ohmic type in LRSs. Very recently, Bersuker suggested that the Ohmic charge transport in the LRS of a TiN/HfO_{2-x}(5 nm)/TiN RRAM cell is caused by the formation of a metallic subband due to high oxygen vacancy concentration.[60]

First-principles simulation using the Vienna *ab initio* simulation package (VASP)[61–64] with the projected augmented wave

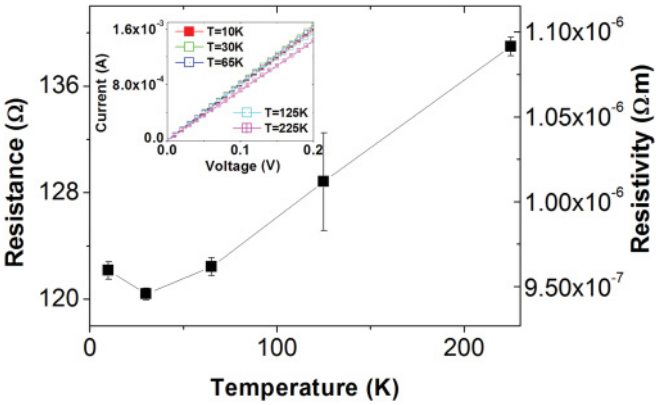

FIG. 5. (Color online) dc resistance and resistivity (by taking film thickness 10 nm and a presumed filament diameter of 10 nm) of the low resistance state cell as a function of temperature (same range), which shows the typical behavior of metal. The inset is the corresponding I-V of a low resistance state at different temperatures T (from 10 to 225 K), which shows a clear Ohmic behavior.

pseudopotential[65] is employed to investigate the electronic structure of the LRS of HfO_{2-x} RRAM. For Hf and O, $5p^6 5d^2 6s^2$ and $2s^2 2p^4$ are treated as the valence electrons, respectively, within the generalized gradient approximation.[66] A plane-wave basis set is used to expand the wave functions of valence electrons with 500 eV energy cutoff. All the lattice parameters and internal coordinates are optimized by the conjugated gradient method until each component of stress tensor is <0.1 GPa, and the forces on each atom are <0.03 eV/Å. Electronic structures associated with the filament of $SrTiO_{3-x}$ and TiO_{2-x} have been tackled by bulk models,[13,18] but the 8-nm-thick HfO_{2-x} dielectric film in our experiment is featured for two preferred facets, $(\bar{1}11)$ and (111), as shown in the XRD measurement of Fig. 1(c). It has been demonstrated that the oxygen vacancies can be more readily generated at the grain boundaries[27] and surfaces.[28] Thus, the surfaces of HfO_{2-x} are expected to play a more significant role than the bulk phase in the conducting filament consisting of oxygen vacancies in the HfO_{2-x} system. At room temperature, the stable phase of HfO_2 is monoclinic, which transforms to the tetragonal phase at 1300 K, then to the cubic phase at near 2700 K.[67] Here we use a surface model of monoclinic HfO_{2-x} with oxygen vacancies to simulate the electronic structure of a LRS. First, we perform *ab initio* calculations for the bulk monoclinic phase of HfO_2. In the monoclinic phase, each Hf atom is coordinated by seven nearest oxygen atoms. As shown in Fig. 6(a), oxygen atoms form alternating three-coordinating and four-coordinating planes along the a direction. The optimized monoclinic cell parameters (a = 5.135 Å, b = 5.205 Å, c = 5.304 Å, and β = 99.6°), the calculated band gap (4.0 eV) and density of states (DOS) are in good agreement with previous studies.[13,68–70]

Secondly, we choose nine inequivalent low-index surfaces of monoclinic HfO_2. The stability of the surface is determined by the surface energy density $\gamma(n)$ of a system comprising n layers as

$$\gamma(n) = \frac{E_{\mathrm{tot}}(n) - E_{\mathrm{bulk}}(n)}{2A}, \quad (14)$$

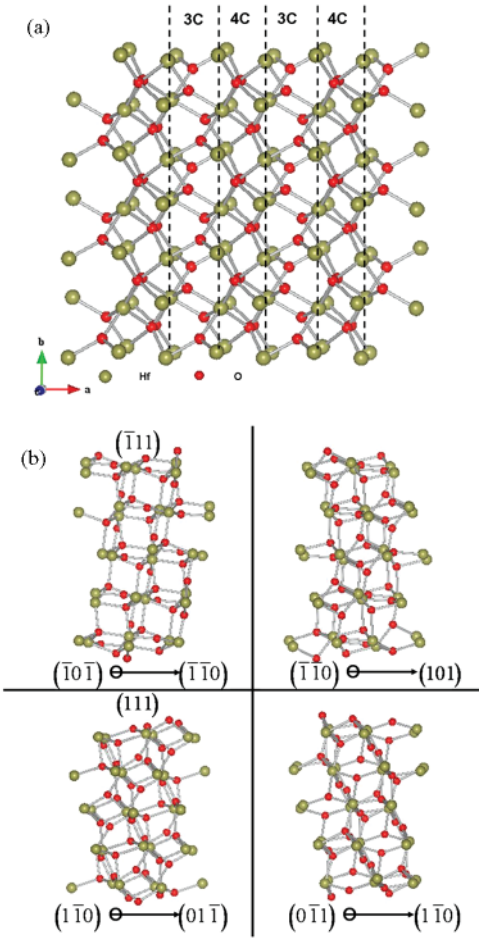

FIG. 6. (Color online) (a) Structure of monoclinic HfO_2; yellow balls represent Hf atoms, while red balls represent O atoms. (b) $(\bar{1}11)$ and (111) slab structures of monoclinic HfO_2.

where $E_{tot}(n)$ and A are the total free energy and surface areas per molecular unit, respectively, while $E_{bulk}(n)$ is the corresponding free energy in the bulk phase, which contains the same molecular units as the slab model.

Table II(a) shows that $(\bar{1}11)$ and (111) surfaces [as shown in Fig. 6(b)] are the most stable surfaces among the low-index surfaces, consistent with the XRD results as shown in Fig. 1(c). The predicted order of stability for HfO_2 is $(\bar{1}11) > (111) > (\bar{1}01) > (110) > (001) > (011) > (101) > (100) > (010)$, which is the same as a previous study.[68] Here we focus on the $(\bar{1}11)$ surface; the formation energy of oxygen vacancies at different distances to the surface is given by Table II(b). Clearly, the four-coordinated oxygen is more likely to be removed from HfO_2 than three-coordinated oxygen, which is irrespective of the vacancy positions.[67,70] This tendency is also consistent with the conclusion derived from the bulk model. Table II(b) also shows that oxygen vacancy on the surface is easier to create than that in the interior due to different bonding environments. The O atoms inside the slab have a similar crystal environment to those in the bulk phase, so the corresponding formation energy approaches that of bulk phase.

The formation of conducting filaments in our study consists of multiple aligned oxygen vacancies on the HfO_{2-x} $(\bar{1}11)$ surface. The energetically favorable [101] directional vacancy chain is created by aligning two three-coordinated and two four-coordinated oxygen vacancies in the $(\bar{1}11)$ slab. As shown in Fig. 7(a), the valence band states are mainly composed of O $2p$ orbitals hybridized with Hf $5d$ orbitals. Surface states locate at the top of the valence band which originates from the dangling bonds of surface oxygen atoms, and thus it is mainly constituted of O $2p$ states. On the other hand, the conduction-band states consist of Hf $5d$ states with weak hybridization with O $2p$ orbitals. The presence of oxygen vacancies introduces intermediate states inside the band gap of bulk HfO_2, which are mainly contributed by $5d$ orbitals from Hf atoms: extra free Hf d electrons stay at the $5d$ orbitals and the Fermi level is pushed up to the valence band; thus the band gap decreases drastically. The decomposition of the wave function indicates that the impurity band is mainly the t_{2g} orbitals of Hf, with a relative larger contribution from the

TABLE II. Calculated surface and formation energies. The $(\bar{1}11)$ surface is of the lowest surface energy, which is consistent with the literature report and XRD observation. Four-coordinated oxygen vacancies are subjected to lower formation energy in both the slab model and the bulk model. Formation energy is lowered in vicinity to the surface.

(a) Calculated surface energy of the nine inequivalent low-index surfaces of monoclinic HfO_2

Surface	Surface energy (J/m^2)	Surface energy [6]
$(\bar{1}11)$	1.015	0.993
(111)	1.193	1.199
$(\bar{1}01)$	1.335	1.322
(110)	1.335	1.388
(001)	1.427	1.416
(011)	1.433	1.484
(101)	1.509	1.550
(100)	1.636	1.667
(010)	1.821	1.878

(b) Calculated formation energy of oxygen vacancies at the $(\bar{1}11)$ phase and bulk phase.

	3-c O-v (eV)	4-c O-v (eV)
Near surface	$7.05 + \Delta\mu_O$	$6.81 + \Delta\mu_O$
In the middle of slab	$7.15 + \Delta\mu_O$	$7.02 + \Delta\mu_O$
Bulk phase	$7.37 + \Delta\mu_O$	$7.22 + \Delta\mu_O$

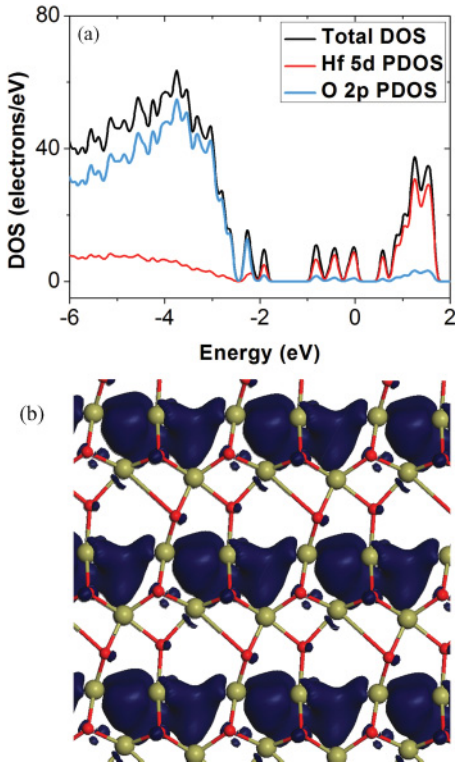

FIG. 7. (Color online) (a) Density of states of $(\bar{1}11)$ slabs with [101] oxygen vacancy chains. The Fermi level is positioned at 0 eV. Extra free Hf d electrons stay at the 5d orbitals and the Fermi level is pushed up to the valence band, resulting in the intermediate states. (b) Illustration of partial charge density (isosurface value $0.07e/\text{Å}^3$) near the Fermi level of $(\bar{1}11)$ slabs with [101] oxygen vacancy chains. The wave functions show the trend of delocalization which may be the origin of the weak metallic nature.

d_{xz} atomic orbital. The overlap of t_{2g} wave functions of two neighboring Hf atoms may create a weak bonding. The partial charge density distribution in the real space near Fermi level, as shown in Fig. 7(b), reveals that the wave function of defect states associated with the [101] vacancy chain is delocalized in contrast to an isolated oxygen vacancy. Hence, electrons are capable of transporting through those oxygen-deprived Hf ions in the [101] direction. This may be a clue for the formation of conduction filament by oxygen vacancies, which is consistent with the impurity band in Fig. 7(a), and provide the percolation path of a charge carrier in the resistive-switching process. We propose that the weak metallic nature of a LRS results from delocalization of the impurity band wave functions associated with aligned oxygen vacancies. The stability of different directional oxygen vacancy chains is compared in terms of formation energy. It has been shown that [101] is more stable than other one-dimensional (1D) low-index oxygen vacancy chains. For instance, the formation energy of the [101] chain is 0.383 eV per formula unit lower than that of the [110] chain, implying that the vacancy chain with a higher 1D vacancy density is much preferred.

IV. CONCLUSIONS

By using dc and low-frequency ac transport measurements at different temperatures, the three states of $Pt/HfO_{2-x}/TiN$ based RRAM have been shown of distinct behaviors. Equivalent circuit models are built for individual states. The conductance of the pristine cell follows the typical power law of polycrystalline/amorphous semiconductors. An additional frequency-independent term is introduced in HRSs and LRSs, and this additional conductance term in a HRS is believed of both the frequency and cross-sectional area independence but strong temperature dependence, which may be related to the partially ruptured oxygen vacancy filament. The dc activation energy is ∼50 meV at temperatures higher than 100 K and 2.1 meV at temperatures below half of the Debye temperature. The HRS dc I-V characteristics can be well fitted with small polaron hopping field dependence at high temperature. These observations may lead to the fact that the HRS conduction is small polaron related, and it is further confirmed by the high-frequency dielectric loss in HRSs. On the contrary, the additional conductance component in a LRS is independent of frequency and cross-sectional areas but slightly dependent on temperature, suggesting a weak metallic nature. The insulator-metal transition is attributed to the high local oxygen vacancy density caused delocalization of the wave functions of the impurity band. To see the properties of oxygen vacancies in polycrystalline material, first-principles simulation has been used to study aligned oxygen vacancy chains on the relatively stable $(\bar{1}11)$ surface. Through analysis of the partial DOS and spatial distribution of the wave functions associated with the impurity states generated by oxygen vacancies, the delocalization of the impurity band is believed to be responsible for the weak metallic LRS.

ACKNOWLEDGMENTS

Work at NTU was supported in part by a MOE AcRF-Tier-1 grant (No. M52070060) and A*STAR SERC grant (No. M47070020).

*yu.hy@sustc.edu.cn; hbsu@ntu.edu.sg

[1] T. W. Hickmott, J. Appl. Phys. **33**, 2669 (1962).
[2] G. Dearnaley, A. M. Stoneham, and D. V. Morgan, Rep. Prog. Phys. **33**, 1129 (1970).
[3] S. R. Ovshinsky and H. Fritzsche, IEEE Trans. Electron Devices **20**, 91 (1973).
[4] A. Beck, J. Bednorz, C. Gerber, C. Rossel, and D. Widmer, Appl. Phys. Lett. **77**, 139 (2000).
[5] C. Rossel, G. I. Meijer, D. Brémaud, and D. Widmer, J. Appl. Phys. **90**, 2892 (2001).
[6] I. G. Baek, M. S. Lee, S. Seo, M. J. Lee, D. H. Seo, D.-S. Suh, J. C. Park, S. O. Park, H. S. Kim, I. K. Yoo, U.-I. Chung, and J. T. Moon, Tech. Dig. - Int. Electron Devices Meet. 2004, p. 587.
[7] H. Y. Lee, P. S. Chen, T. Y. Wu, Y. S. Chen, C. C. Wang, P. J. Tzeng, C. H. Lin, F. Chen, C. H. Lien, and M.-J. Tsai, Tech. Dig. - Int. Electron Devices Meet. 2008, p. 1.

[8] Y. Watanabe, J. G. Bednorz, A. Bietsch, C. Gerber, D. Widmer, A. Beck, and S. J. Wind, Appl. Phys. Lett. **78**, 3738 (2001).

[9] A. Baikalov, Y. Q. Wang, B. Shen, B. Lorenz, S. Tsui, Y. Y. Sun, Y. Y. Xue, and C. W. Chu, Appl. Phys. Lett. **83**, 957 (2003).

[10] N. Das, S. Tsui, Y. Xue, Y. Q. Wang, and C. W. Chu, Phys. Rev. B **78**, 235418 (2008).

[11] N. Xu, L. Liu, X. Sun, X. Liu, D. Han, Y. Wang, R. Han, J. Kang, and B. Yu, Appl. Phys. Lett. **92**, 232112 (2008).

[12] D.-H. Kwon, K. M. Kim, J. H. Jang, J. M. Jeon, M. H. Lee, G. H. Kim, X.-S. Li, G.-S. Park, B. Lee, S. Han, M. Kim, and C. S. Hwang, Nat. Nanotechnol. **5**, 148 (2010).

[13] S.-G. Park, B. Magyari-Köpe, and Y. Nishi, IEEE Electron Device Lett. **32**, 197 (2011).

[14] L. Goux, P. Czarnecki, Y. Y. Chen, L. Pantisano, X. P. Wang, R. Degraeve, B. Govoreanu, M. Jurczak, D. J. Wouters, and L. Altimime, Appl. Phys. Lett. **97**, 243509 (2010).

[15] I. K. Yoo, B. S. Kang, S. E. Ahn, C. B. Lee, M. J. Lee, G.-S. Park, and X.-S. Li, IEEE Trans. Nanotechnol. **9**, 131 (2010).

[16] H. Kondo, M. Arita, T. Fujii, H. Kaji, M. Moniwa, T. Yamaguchi, I. Fujiwara, M. Yoshimaru, and Y. Takahashi, Jpn. J. Appl. Phys. **50**, 081101 (2011).

[17] X. Li, C. H. Tung, and K. L. Pey, Appl. Phys. Lett. **93**, 072903 (2008).

[18] K. Szot, W. Speier, G. Bihlmayer, and R. Waser, Nat. Mater. **5**, 312 (2006).

[19] H. K. Gun, H. L. Jong, Y. S. Jun, J. S. Seul, H. Y. Jung, J. Y. Kyung, H. L. Min, M. K. Kyung, D. L. Hyung, W. R. Seung, J. P. Tae, and S. H. Cheol, Appl. Phys. Lett. **98**, 262901 (2011).

[20] X. Du, Q. Li, H. Su, and J. Yang, Phys. Rev. B **74**, 233201 (2006).

[21] H. Su, D. Welch, and W. Wong-Ng, Phys. Rev. B **70**, 054517 (2004).

[22] R. Waser, R. Dittmann, G. Staikov, and K. Szot, Adv. Mater. **21**, 2632 (2009).

[23] H. Akinaga and H. Shima, Proc. IEEE **98**, 2237 (2010).

[24] C. Kügeler, R. Rosezin, E. Linn, R. Bruchhaus, and R. Waser, Appl. Phys. A **102**, 791 (2011).

[25] K. Szot, M. Rogala, W. Speier, Z. Klusek, A. Besmehn, and R. Waser, Nanotechnology **22**, 254001 (2011).

[26] Y.-M. Kim and J.-S. Lee, J. Appl. Phys. **104**, 114115 (2008).

[27] K. McKenna and A. Shluger, Appl. Phys. Lett. **95**, 222111 (2009).

[28] E. Cho, B. Lee, C.-K. Lee, S. Han, S. H. Jeon, B. H. Park, and Y.-S. Kim, Appl. Phys. Lett. **92**, 233118 (2008).

[29] H. Su and D. O. Welch, Supercond. Sci. Technol. **18**, 24 (2005).

[30] D. Muñoz Ramo, A. L. Shluger, J. L. Gavartin, and G. Bersuker, Phys. Rev. Lett. **99**, 155504 (2007).

[31] J. L. Gavartin, D. M. Ramo, A. Shluger, and G. Bersuker, ECS Trans. **3**, 277 (2006).

[32] C. Jorel, C. Vallée, E. Gourvest, B. Pelissier, M. Kahn, M. Bonvalot, and P. Gonon, J. Vac. Sci. Technol. B **27**, 378 (2009).

[33] J. Ni, Q. Zhou, Z. Li, and Z. Zhang, Appl. Phys. Lett. **93**, 011905 (2008).

[34] Z. Fang, H. Y. Yu, W. J. Liu, Z. R. Wang, X. A. Tran, B. Gao, and J. F. Kang, IEEE Electron Device Lett. **31**, 476 (2010).

[35] A. R. Long, Adv. Phys. **31**, 553 (1982).

[36] S. R. Elliott, Adv. Phys. **36**, 135 (1987).

[37] B. Lee, T. Moon, T.-G. Kim, D.-K. Choi, and B. Park, Appl. Phys. Lett. **87**, 012901 (2005).

[38] P. Gonon, M. Mougenot, C. Vallée, C. Jorel, V. Jousseaume, H. Grampeix, and F. El Kamel, J. Appl. Phys. **107**, 074507 (2010).

[39] D. S. Jeong, H. Schroeder, and R. Waser, Appl. Phys. Lett. **89**, 082909 (2006).

[40] M. Pollak and T. H. Geballe, Phys. Rev. **122**, 1742 (1961).

[41] G. E. Pike, Phys. Rev. B **6**, 1572 (1972).

[42] A. K. Jonscher, Nature (London) **253**, 717 (1975).

[43] S. Hazra, A. Ghosh, and D. Chakravorty, J. Phys.: Condens. Matter **8**, 10279 (1996).

[44] J. Bahadur, D. Sen, S. Mazumder, R. Shukla, and A. K. Tyagi, J. Phys.: Condens. Matter **20**, 345201 (2008).

[45] D. Emin, Phys. Rev. B **46**, 9419 (1992).

[46] J. Lee, J. Shin, D. Lee, W. Lee, S. Jung, M. Jo, J. Park, K. P. Biju, S. Kim, S. Park, and H. Hwang, Tech. Dig. - Int. Electron Devices Meet. 2010, p. 19.5.1.

[47] C. Papagianni, Y. B. Nian, Y. Q. Wang, N. J. Wu, and A. Ignatiev, Non-Volatile Memory Technology Symposium, 2004, p. 125.

[48] Y.-H. You, B.-S. So, J.-H. Hwang, W. Cho, S. S. Lee, T.-M. Chung, C. G. Kim, and K.-S. An, Appl. Phys. Lett. **89**, 222105 (2006).

[49] M. H. Lee, K. M. Kim, G. H. Kim, J. Y. Seok, S. J. Song, J. H. Yoon, and C. S. Hwang, Appl. Phys. Lett. **96**, 152909 (2010).

[50] R. G. Southwick, J. Reed, C. Buu, H. Bui, R. Butler, G. Bersuker, and W. B. Knowlton, International Integrated Reliability Workshop, 2008, p. 48.

[51] C. Walczyk, C. Wenger, R. Sohal, M. Lukosius, A. Fox, J. Dąbrowski, D. Wolansky, B. Tillack, H. J. Müssig, and T. Schroeder, J. Appl. Phys. **105**, 114103 (2009).

[52] C. M. Compagnoni, A. S. Spinelli, A. Bianchini, A. L. Lacaita, S. Spiga, G. Scarel, C. Wiemer, and M. Fanciulli, Appl. Phys. Lett. **89**, 103504 (2006).

[53] A. Yildiz, F. Iacomi, and D. Mardare, J. Appl. Phys. **108**, 083701 (2010).

[54] P. Broqvist and A. Pasquarello, Appl. Phys. Lett. **89**, 262904 (2006).

[55] J. Schnakenberg, Phys. Status Solidi B **28**, 623 (1968).

[56] C. G. Jacobs and N. Hershkowitz, Phys. Rev. B **1**, 839 (1970).

[57] D. Emin, Phys. Rev. Lett. **100**, 166602 (2008).

[58] F. Pan, S. Yin, and V. Subramanian, IEEE Electron Device Lett. **32**, 949 (2011).

[59] C. H. Ho, E. K. Lai, M. D. Lee, C. L. Pan, Y. D. Yao, K. Y. Hsieh, R. Liu, and C. Y. Lu, Dig. Tech. Pap. - Symp. VLSI Technol. 2007, p. 228.

[60] G. Bersuker, D. C. Gilmer, D. Veksler, P. Kirsch, L. Vandelli, A. Padovani, L. Larcher, K. McKenna, A. Shluger, V. Iglesias, M. Porti, and M. Nafría, J. Appl. Phys. **110**, 124518 (2011).

[61] G. Kresse and J. Hafner, Phys. Rev. B **47**, 558 (1993).

[62] G. Kresse and J. Hafner, Phys. Rev. B **49**, 14251 (1994).

[63] G. Kresse and J. Furthmüller, Comput. Mater. Sci. **6**, 15 (1996).

[64] G. Kresse and J. Furthmüller, Phys. Rev. B **54**, 11169 (1996).

[65] P. E. Blöchl, Phys. Rev. B **50**, 17953 (1994).

[66] J. P. Perdew, J. A. Chevary, S. H. Vosko, K. A. Jackson, M. R. Pederson, D. J. Singh, and C. Fiolhais, Phys. Rev. B **46**, 6671 (1992).

[67] A. S. Foster, F. Lopez Gejo, A. L. Shluger, and R. M. Nieminen, Phys. Rev. B **65**, 174117 (2002).

[68] A. B. Mukhopadhyay, J. F. Sanz, and C. B. Musgrave, Phys. Rev. B **73**, 115330 (2006).

[69] R. E. Hann, P. R. Suitch, and J. L. Pentecost, J. Am. Ceram. Soc. **68**, C-285 (1985).

[70] J. X. Zheng, G. Ceder, T. Maxisch, W. K. Chim, and W. K. Choi, Phys. Rev. B **75**, 104112 (2007).